

Using a quantum SWAP engine to experimentally validate thermodynamic uncertainty relations

Krishna Shende,^{1,*} Arvind,^{1,†} and Kavita Dorai^{1,‡}

¹*Department of Physical Sciences, Indian Institute of Science Education & Research Mohali, Sector 81 SAS Nagar, Manauli PO 140306 Punjab India.*

Thermodynamic uncertainty relations (TURs) arise from the bounds on fluctuations of thermodynamics quantities during a non-equilibrium process and they impose constraints on the corresponding process. We experimentally implement a quantum SWAP engine on a nuclear magnetic resonance setup and demonstrate that a Gibbs thermal state can be prepared in two different ways, either directly from a thermal equilibrium state, or by first initializing the system in a pseudopure state. We show that the quantum SWAP engine can work both as a heat engine and as a refrigerator. Starting from a pseudopure state, we construct the SWAP engine, and investigate the violation of two different TURs, namely a generalized TUR and a tighter, more specific TUR. Our results validate that the generalized TUR is obeyed in all the working regimes of the SWAP engine, while the tighter TUR is violated in certain regimes.

I. INTRODUCTION

Substantial progress has been made in the field of non-equilibrium quantum thermodynamics over the past two decades, which has led to an understanding of the thermodynamic properties of systems at the microscopic level [1, 2]. Recently, experimental quantum heat engines have been implemented on different quantum platforms [3, 4]. At the microscopic level, apart from thermal fluctuation, quantum fluctuations also influence system dynamics and the non-equilibrium entropy production in a quantum heat engine becomes stochastic in nature, leading to the entropy (Σ) becoming a stochastic variable. These distributions follow symmetry relations, known as fluctuation theorems (FT) [5–9], having a general form $\frac{P(\Sigma)}{P(-\Sigma)} = e^\Sigma$, where $P(\Sigma)$ and $P(-\Sigma)$ are the probability distributions for forward and backward (time reversed) processes, respectively. FTs have been studied using various experimental setups such as nuclear magnetic resonance (NMR)[10–13], ion traps [14] and nitrogen vacancy (NV) centers[15].

Another set of powerful inequalities known as thermodynamic uncertainty relations (TURs) were formulated, which impose restrictions on fluctuations in various thermodynamic quantities in terms of the irreversible entropy produced during a non-equilibrium process [16, 17]. For a Markovian system with N discrete states, the rates of transitions between neighboring states fulfill the local detailed balance equation [18]. In such scenarios the integrated thermodynamic current Q_i (for instance, such currents could arise from chemical potential differences in biomolecular reactions or colloidal forces etc.) exchanged during an out-of-equilibrium process for some definite time interval, is bounded by the corresponding

TUR (termed TUR-1) [16]:

$$\frac{\text{Var}(Q_i)}{\langle Q_i \rangle^2} \geq \frac{2}{\langle \Sigma \rangle} \quad (1)$$

where $\text{Var}(Q_i) = \langle Q_i^2 \rangle - \langle Q_i \rangle^2$ is the variance, and $\langle \Sigma \rangle$ is the average entropy produced during an out-of-equilibrium process and also quantifies how far the system is driven away from equilibrium. TUR-1 (Eq. 1) implies a trade-off relation between the precision i.e. the variance in integrated current, and the average entropy produced. Hence, to reduce fluctuations, one must pay the inevitable price of entropy production [19].

The conditions used to derive the TUR-1 bound exclude some key system dynamics such as systems driven by a time-dependent protocol, microscopic heat engines, and quantum non-equilibrium dynamics [20–22]. Hence, a tighter TUR was derived (termed TUR-2) assuming an exchange fluctuation theorem (XFT) scenario [23]:

$$\frac{\text{Var}(Q_i)}{\langle Q_i \rangle^2} \geq f(\langle \Sigma \rangle) \quad (2)$$

where $f(x) = \text{cosech}^2[g(x/2)]$, and $g(x)$ is the inverse function of $x \tanh(x)$. In the XFT scenario, a system can comprise N subsystems, each initially prepared at different inverse temperatures and different chemical potentials. These subsystems are brought in contact with each other via a unitary operator U which facilitates all types of interactions such that the subsystems can exchange net current, energies and particles with each other. TURs have been recently studied experimentally in the heat exchange case [24], where two qubits initially prepared at different spin temperature interacted via an external driving unitary, such that heat is exchanged between the qubits. A series expansion of $f(\langle \Sigma \rangle)$ around $\langle \Sigma \rangle = 0$ gives $f(\langle \Sigma \rangle) \approx 2/\langle \Sigma \rangle - 2/3$ [23]. Consequently, TUR-2 (Eq. 2) simplifies to TUR-1 (Eq. 1) when entropy values are minimal ($\langle \Sigma \rangle \rightarrow 0$).

Quantum engines can be used to examine various thermodynamic properties at the quantum level and three

* ph19032@iisermohali.ac.in

† arvind@iisermohali.ac.in

‡ kavita@iisermohali.ac.in

types of quantum engines have been proposed in the literature [25, 26]: (i) a 4-stroke heat engine also known as Otto engine, (ii) a 2-stroke heat engine also called the SWAP engine, and (iii) a continuous heat engine. Different types of quantum engines have been experimentally implemented on NMR quantum processors [27–29] NV centers [30], in a trapped-ion setup [31, 32] and using superconducting qubits [33]. The smallest possible refrigerator was recently built using three NMR qubits which operates without relying on net external work [34]. A SWAP quantum engine was implemented on a cloud quantum processor which has a boosted efficiency above the standard Carnot limit [35].

In this work, we experimentally demonstrate the implementation of a quantum SWAP engine [36] on a two-qubit NMR quantum processor. We show that the quantum SWAP engine can be constructed in two different ways, by starting from a thermal equilibrium state, or by first preparing the system in a pseudopure state. We observe the working of the SWAP engine as a heat engine and as a refrigerator, depending on the spin temperature and the energy gap of the qubits. The spin temperature of one qubit is held fixed at two different values and the spin temperature of the other qubit is changed in order to probe the dynamics of the engine. We use the quantum SWAP engine to explore the validity of the TUR-1 and TUR-2 bounds in different operation modes of the quantum SWAP engine.

This paper is organized as follows: The theoretical framework of the quantum SWAP engine is explained in Section II, with a detailed calculation of its working principle and required quantities. Section III describes the NMR experimental setup and contains details about the implementation of the quantum SWAP engine on a two-qubit NMR platform. Section IV contains a discussion of the experimental study of the TURs using a quantum SWAP engine. Section V offers some concluding remarks.

II. THEORETICAL BACKGROUND

We briefly describe the operational aspects of a quantum SWAP engine and its implementation on an NMR quantum processor and also provide definitions of the quantities required for computing the TURs.

A. NMR SWAP Engine

Consider two NMR qubits (denoted by qubit 1 and qubit 2) with an energy level spacing of ϵ_1 and ϵ_2 , respectively. Two heat baths are initialized to different spin temperatures, such that $\beta_2 \leq \beta_1$, i.e. the first bath is colder than the second. A schematic diagram of this two-qubit SWAP engine is shown in Figure 1, with different energy gaps and initial temperatures. The working of this engine is carried out in two steps, termed as the first

and second stroke, respectively (shown in Figures 1(a) and (b)).

First stroke of the SWAP engine: During the execution of the first stroke of the engine, the qubits with Zeeman Hamiltonians $H_1 = -h\epsilon_1 I_z$ and $H_2 = -h\epsilon_2 I_z$ are initialized to different temperatures via equilibration with their respective heat baths. The composite system is in a diagonal state given by $\rho_i = \exp[-\beta_i H_i]/Z_i$, which is a Gibbs state given by[9]:

$$\rho^{(a)} = \rho_1^{(a)} \otimes \rho_2^{(a)} = e^{-\frac{\beta_1 H_1}{Z_1}} \otimes e^{-\frac{\beta_2 H_2}{Z_2}} \quad (3)$$

where the superscript a refers to the first stroke of the engine, and $\beta_i = 1/(k_B T_i)$ and $Z_i = \text{Tr}[\exp(-\beta_i H_i)]$ are the inverse spin temperature and the partition function of the i^{th} qubit, respectively.

The initial density operator of each qubit is given by:

$$\begin{aligned} \rho_1^{(a)} &= \frac{1}{Z_1} \{ |0\rangle_1 \langle 0|_1 + e^{-\beta_1 \epsilon_1} |1\rangle_1 \langle 1|_1 \} \\ \rho_2^{(a)} &= \frac{1}{Z_2} \{ |0\rangle_2 \langle 0|_2 + e^{-\beta_2 \epsilon_2} |1\rangle_2 \langle 1|_2 \} \end{aligned} \quad (4)$$

where $\beta_{1(2)} = 1/k_B T_{1(2)}$ and for simplicity the eigen energy of the ground state has been chosen as a reference point [25].

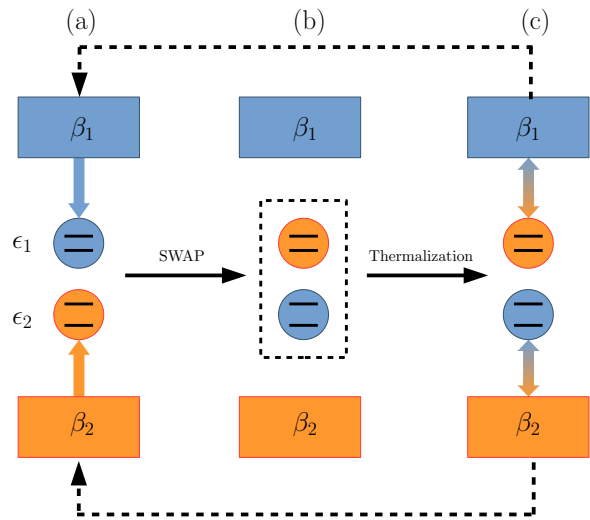


FIG. 1. Schematic diagram showing operation of the quantum SWAP engine in the heat engine mode. (a) The two qubits are thermalized to their respective baths, with $\beta_1 \geq \beta_2$ and $\epsilon_2 > \epsilon_1$. (b) Both the qubits are decoupled from their baths and allowed to interact with each other via a SWAP operation. (c) The qubits are once again thermalized with their respective baths, to begin a new thermodynamic cycle.

Second stroke of the SWAP engine: During the second stroke of the SWAP engine, both qubits are disconnected from their heat baths, and the qubits are allowed to interact via a quantum SWAP unitary U gate given

by:

$$U = \begin{bmatrix} 1 & 0 & 0 & 0 \\ 0 & 0 & 1 & 0 \\ 0 & 1 & 0 & 0 \\ 0 & 0 & 0 & 1 \end{bmatrix} \quad (5)$$

which exchanges the states of both the qubits [37]. The density operator for each qubit after the SWAP gate operation is given by:

$$\begin{aligned} \rho_1^{(b)} &= \frac{1}{Z_2} \{ |0\rangle_1 \langle 0|_1 + e^{-\beta_2 \epsilon_2} |1\rangle_1 \langle 1|_1 \} \\ \rho_2^{(b)} &= \frac{1}{Z_1} \{ |0\rangle_2 \langle 0|_2 + e^{-\beta_1 \epsilon_1} |1\rangle_2 \langle 1|_2 \} \end{aligned} \quad (6)$$

where the superscript b refers to the second stroke of the engine. After this, the qubits are once again allowed to equilibrate with their respective heat baths, in order to begin a new thermodynamic cycle (Figure 1(c)). The change in the energy of each qubit is given by:

$$\langle \Delta E_i \rangle = \text{Tr}[H_i(\rho^{(b)} - \rho^{(a)})] \quad (7)$$

where H_i is the Hamiltonian of i^{th} qubit. The average work done is given by:

$$\langle W \rangle = \langle \Delta E_1 \rangle + \langle \Delta E_2 \rangle \quad (8)$$

The first stroke of the SWAP engine wherein both qubits are thermalized, is equivalent to two quantum isochoric processes, while the SWAP operation which is implemented during the second stroke of the SWAP engine can be regarded as two quantum adiabatic steps, when the work is done. During the thermalization process, the energy change in each individual qubit due to the second stroke of the engine is dumped in its respective heat bath. This energy change can be related to the heat flow of the individual qubits as $Q_1 = -\langle \Delta E_1 \rangle$ and $Q_2 = -\langle \Delta E_2 \rangle$.

The heat absorbed by qubit 1 is given by[25, 36]:

$$\begin{aligned} Q_1 &= -\langle \Delta E_1 \rangle = \text{Tr}[H_1(\rho_1^{(b)} - \rho_1^{(a)})] \\ &= -\epsilon_1 \left[\frac{e^{-\beta_2 \epsilon_2}}{Z_2} - \frac{e^{-\beta_1 \epsilon_1}}{Z_1} \right] \end{aligned} \quad (9)$$

The heat released by qubit 2 is given by [25, 36]:

$$\begin{aligned} Q_2 &= -\langle \Delta E_2 \rangle = \text{Tr}[H_2(\rho_2^{(b)} - \rho_2^{(a)})] \\ &= -\epsilon_2 \left[\frac{e^{-\beta_1 \epsilon_1}}{Z_1} - \frac{e^{-\beta_2 \epsilon_2}}{Z_2} \right] \\ &= \epsilon_2 \left[\frac{e^{-\beta_2 \epsilon_2}}{Z_2} - \frac{e^{-\beta_1 \epsilon_1}}{Z_1} \right] \end{aligned} \quad (10)$$

The extracted work is given by[25, 36]:

$$\begin{aligned} W &= \langle \Delta E_1 \rangle + \langle \Delta E_2 \rangle = -(Q_1 + Q_2) \\ &= (\epsilon_2 - \epsilon_1) \left[\frac{e^{-\beta_2 \epsilon_2}}{Z_2} - \frac{e^{-\beta_1 \epsilon_1}}{Z_1} \right] \end{aligned} \quad (11)$$

The difference in the average energy change of each qubit gives the work, and also gives the direction of heat flow. The system can work either as an engine or as a refrigerator depending on whether the heat flows from the hot to the cold qubit or vice versa. The quantity Q_i is positive if heat flows out from a qubit and negative if heat is gained by the qubit. It can be inferred from the above equations that, if both the qubits have the same energy gap, the work done is always zero. Hence, for any quantum system to work as a SWAP engine, both the qubits must have different energy gaps.

The quantum SWAP heat engine efficiency is computed to be[23, 36]:

$$\eta = -\frac{W}{Q_2} = 1 - \frac{\epsilon_1}{\epsilon_2} \quad (12)$$

When heat flows from a cold to a hot reservoir, the system works as a refrigerator ($W > 0$) and work is done on the system. The system works as a heat engine when work ($W < 0$) is extracted from it. The conditions for the working of a quantum SWAP engine are delineated below [23, 36]:

- Heat engine: $1 > \frac{\epsilon_1}{\epsilon_2} > \frac{\beta_2}{\beta_1}$
- Refrigerator: $\frac{\beta_2}{\beta_1} > \frac{\epsilon_1}{\epsilon_2} > 0$

B. Average Entropy and variance

The central quantities required to explore TURs (Eq. 1 and Eq. 2) in different working regimes of the quantum SWAP engine are the variances of heat and work, and the average entropy produced when the system goes to a non-equilibrium state. A TUR places a restriction on the uncertainty (variance) in the integrated current in terms of entropy produced. Hence, if one wants to decrease this uncertainty, one has to pay the inevitable price of more entropy production.

The average entropy produced by a SWAP engine is given by [23]:

$$\langle \Sigma \rangle = (\beta_1 - \beta_2) \langle Q \rangle - \beta_1 \langle W \rangle \quad (13)$$

where $\langle Q \rangle$ and $\langle W \rangle$ are the average released heat and average extracted work as given in Eq. 10 and Eq. 11, respectively. We denote the heat released from qubit 2 (Q_2) as Q . The variance of any quantity denotes the deviation from its mean value. The variances of heat and work and all their cumulants can be computed from the cumulant generating function to be [23]:

$$\text{Var}(Q)/2 = \frac{2\epsilon_1^2 e^{\beta_2 \epsilon_2}}{(1 + e^{\beta_2 \epsilon_2})(1 + e^{\beta_1 \epsilon_1})} + \frac{\epsilon_1 Q_2}{1 + e^{\beta_1 \epsilon_1}} + \frac{\epsilon_1 Q_2 e^{\beta_2 \epsilon_2}}{1 + e^{\beta_2 \epsilon_2}} \quad (14)$$

$$\begin{aligned} \text{Var}(W)/2 = & \frac{2(\epsilon_1 e^{\beta_1 \epsilon_1} + \epsilon_2)(\epsilon_2 e^{\beta_2 \epsilon_2} + \epsilon_1)}{(1 + e^{\beta_2 \epsilon_2})(1 + e^{\beta_1 \epsilon_1})} - \frac{(\epsilon_1 e^{\beta_1 \epsilon_1} + \epsilon_2)W}{1 + e^{\beta_1 \epsilon_1}} - \frac{(\epsilon_2 e^{\beta_2 \epsilon_2} + \epsilon_1)W}{1 + e^{\beta_2 \epsilon_2}} \\ & + \frac{\epsilon_1^2 e^{\beta_1 \epsilon_1} + \epsilon_2^2}{1 + e^{\beta_1 \epsilon_1}} + \frac{\epsilon_2^2 \exp(\beta_2 \epsilon_2) + \epsilon_1^2}{1 + e^{\beta_2 \epsilon_2}} - (\epsilon_1 + \epsilon_2) \frac{(\epsilon_1 e^{\beta_1 \epsilon_1} + \epsilon_2)}{1 + e^{\beta_1 \epsilon_1}} - (\epsilon_1 + \epsilon_2) \frac{(\epsilon_2 e^{\beta_2 \epsilon_2} + \epsilon_1)}{1 + e^{\beta_2 \epsilon_2}} \end{aligned} \quad (15)$$

where β_1 and β_2 are the inverse spin temperatures of qubit 1 and qubit 2 and ϵ_1 and ϵ_2 are the energy gaps of qubit 1 and qubit 2, respectively.

Recently, a novel identity connecting the inverse signal-to-noise ratio between heat and work has been identified, specifically in the context of the SWAP engine [38]:

$$\frac{\text{Var}(Q)}{\langle Q \rangle^2} = \frac{\text{Var}(W)}{\langle W \rangle^2} \quad (16)$$

which implies that the inverse signal-to-noise ratio of heat and work are equal. The difference between the average value of work and heat is compensated for by having more uncertainty in either work or heat, such that the inverse signal-to-noise ratio of heat and work remains the same. All the above relations (Eqn. 9-16) capture the interdependence among heat, work and entropy production.

III. EXPERIMENTAL IMPLEMENTATION

A ^{13}C -labeled chloroform molecule dissolved in Acetone-D6 was used to realize a two-qubit system, where the ^1H and ^{13}C spins are encoded as qubit 1 and qubit 2, respectively (the molecular structure and experimental parameters are depicted in Figure 2). Experiments were performed on a Bruker Avance III 600 MHz NMR spectrometer equipped with a 5 mm TXI probe. The NMR Hamiltonian for a two-qubit system is given by [39, 40]:

$$\mathcal{H} = - \sum_{i=1}^2 \frac{h\nu_i}{2} \sigma_z^i + \sum_{i < j=1}^2 \frac{hJ_{ij}}{4} \sigma_z^i \sigma_z^j \quad (17)$$

where ν_i the offset frequency, σ_z^i is the z component of the spin angular momentum and J_{ij} is the scalar coupling between spins i and j , respectively. The Hamiltonians H_1 and H_2 in Eq. 3 can be realized from the Hamiltonian in Eq. 17 as $H_1 = \frac{-h\nu_1}{2} \sigma_z^1$ and $H_2 = \frac{-h\nu_2}{2} \sigma_z^2$, where $\nu_1 = 4785.59$ Hz and $\nu_2 = 11812.91$ Hz, respectively.

The quantum circuit to implement the SWAP engine is shown in Figure 3. Single-qubit rotation gates are implemented via high-power rf pulses of short duration. The system is allowed to freely evolve under the Hamiltonian during time periods when no pulses are applied; evolution periods are interspersed with π pulses to refocus chemical

shifts and retain only the desired scalar coupling interactions. For ^1H and ^{13}C spins, the duration of $\frac{\pi}{2}$ pulses are 7.2 μs and 12.80 μs at power levels of 19.9 W and 237.3 W, respectively. The spin-lattice and spin-spin relaxation times of both qubits are much longer than the gate implementation times and hence do not affect the overall experimental performance.

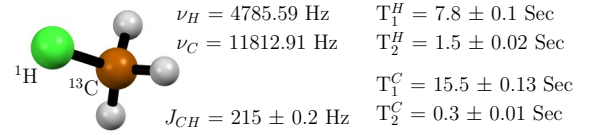


FIG. 2. Molecular structure of ^{13}C -labeled CHCl_3 with the two qubits being realized by the ^1H and ^{13}C spins. The offset rotation frequencies (ν), the scalar coupling strength (J) and the T_1 and T_2 relaxation times for each qubit are shown alongside.

The implementation of the quantum SWAP engine can be divided into two parts: (i) the initial thermalization into the Gibbs state and (ii) the SWAP operation during which the work is done. The effective spin temperature (β_i) of the initial Gibbs state is related to the ground (p_0) and excited (p_1) populations as [25]:

$$\beta_i = \frac{1}{h\nu} \ln \left(\frac{p_0}{p_1} \right) \quad (18)$$

where h is Planck's constant and ν is the offset frequency.

We have implemented the first stroke of the engine using two different schemes, which we call the (i) Direct SWAP engine and the (ii) PPS SWAP engine, respectively. The circuit and pulse sequence to realize the direct SWAP engine are shown in Figure 3(a) and (b), respectively. The circuit and pulse sequence inside the pink shaded boxes are not implemented and only the circuit and pulse sequence within the two black vertical lines are used. The magnetization strength is varied by applying strong rf pulses along the y -axis, of flip angles ranging between 0° to 90° , on both the qubits. The angle of rotation of these pulses controls the ratio of the population between the ground and excited states. This leads to a redistribution of populations in the energy states of the spins and the effective spin temperature of the nuclei is changed accordingly. Any residual coherence

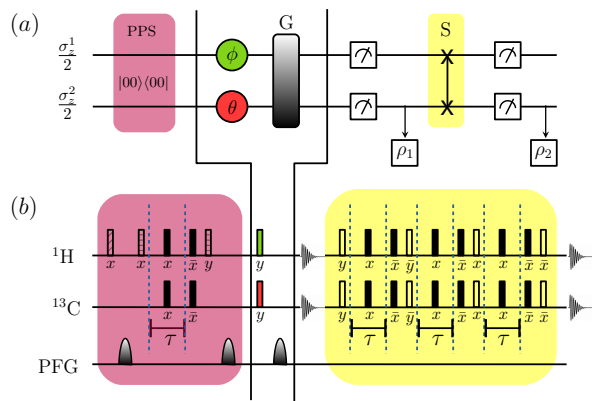


FIG. 3. (a) Quantum circuit to implement a two-qubit quantum SWAP engine. The first box represents PPS state preparation. The green and red circles represent transverse rf pulse along the y -axis and the values of θ and ϕ control the spin population (which is directly proportional to its spin temperature). (b) NMR pulse sequence to realize the quantum SWAP heat engine. Bars with diagonal lines, bars with horizontal lines, unfilled bars and bars having crosshatched lines represent rf pulses of flip angle $(\frac{\pi}{3})$, $(\frac{\pi}{4})$, (π) and $(\frac{\pi}{2})$, respectively. The phases of the rf pulses are written below their respective bars. Grey and black bars correspond to pulses of angles (ϕ) and (θ) , respectively. The line denoted by ‘PFG’ depicts the times at which a pulsed field gradient magnetic pulse is employed to destroy coherence. The time interval τ is set equal to $\frac{1}{2J_{CH}}$.

in the system is killed by applying pulsed field gradient pulses along the z -axis. Quantum state tomography is then performed using the constrained convex optimization approach [41], to reconstruct the density operator ρ_1 , corresponding to the initial Gibbs state.

In the scheme to implement the PPS SWAP engine, the initial thermalization to the Gibbs state at different spin temperatures is achieved by first preparing the system in a pseudopure state (PPS) using the spatial averaging technique and pulsed field gradients:

$$\rho_{PPS} = \frac{1}{4}(1 - \eta)I + \eta|00\rangle\langle 00|. \quad (19)$$

where η is a factor proportional to the spin polarization which depends on the external magnetic field and the gyromagnetic ratio. The initial thermalization is achieved by implementing the circuit before the first vertical black line in Figure 3(b). The rest of the PPS SWAP engine implementation proceeds as described above for the direct SWAP engine.

The second stroke of the engine consists of the quantum SWAP gate and is implemented experimentally using the part of the NMR pulse sequence after the second vertical black line in Figure 3(b). Quantum state tomography is once again performed to reconstruct the final density operator ρ_2 , after the second stroke of the engine. This completes one full thermodynamic cycle of the heat engine. A new thermodynamic cycle is begun

by letting each spin relax to its thermal equilibrium state by waiting $6.5 \times T_1$ of the spins.

The density operator ρ_1 and ρ_2 are used to evaluate average heat, work and Σ as given in Eq.10, Eq.11 and Eq.13. The closeness between the theoretically predicted density operator (ρ_t) and the experimentally reconstructed density operator (ρ_e) is characterized by the fidelity [42]:

$$F = \frac{|Tr(\rho_e \rho_t^\dagger)|}{\sqrt{Tr(\rho_e \rho_e^\dagger)Tr(\rho_t \rho_t^\dagger)}} \quad (20)$$

All the experimental states were reconstructed with an excellent fidelity of $\approx 99\%$.

IV. RESULTS AND DISCUSSION

A. Direct SWAP Engine Dynamics

The direct SWAP engine was experimentally realized using the pulse sequence given in Figure 3(b) (skipping elements in the pink colored box). The spin temperature of the first qubit was kept fixed at $\beta_1 h = 1.61 \times 10^{-10}$ kHz $^{-1}$ (300 K), while the spin temperature of second qubit was varied from $\beta_2 h = 1.2 \times 10^{-10}$ kHz $^{-1}$ (400 K) to $\beta_2 h = 1.25 \times 10^{-9}$ kHz $^{-1}$ (1200 K). The plots for entropy production, heat and extracted work are shown in Figure 4. It is evident from the plots that for certain values of spin temperature, the direct SWAP engine works as a heat engine and as a refrigerator for other spin temperatures. These working regimes are separated by the black dashed vertical line as shown in Figure 4(a). Theoretically computed average heat and work are shown as solid teal and dashed purple lines in Figure 4(a), while the experimentally obtained values (along with error bars) are depicted as teal crosses and purple circles, respectively. There is a very good agreement between the theoretical and experimental values. The average entropy after each thermodynamic cycle for a given value of spin temperature of both the qubits is shown in Figure 4(b). The solid green curve is the theoretically predicted value while the green diamonds are the experimentally obtained values of average entropy. The average entropy becomes zero when the condition $\frac{\epsilon_1}{\epsilon_2} = \frac{\beta_2}{\beta_1}$ is satisfied. For this condition, the average heat and work becomes zero, which leads to zero entropy production. If we move away from this condition, the average entropy production is non-zero and it increases depending upon how far the system is from equilibrium. We observed that $\langle \Sigma \rangle \geq 0$, which follows from the second law of thermodynamics. As observed in Figure 4(b), the average entropy produced by the direct SWAP engine is of the order of 10^{-9} . For such low entropy values, the inverse signal-to-noise ratio and the RHS of TUR-1(Eq. 1) and TUR-2(Eq. 2) become equal.

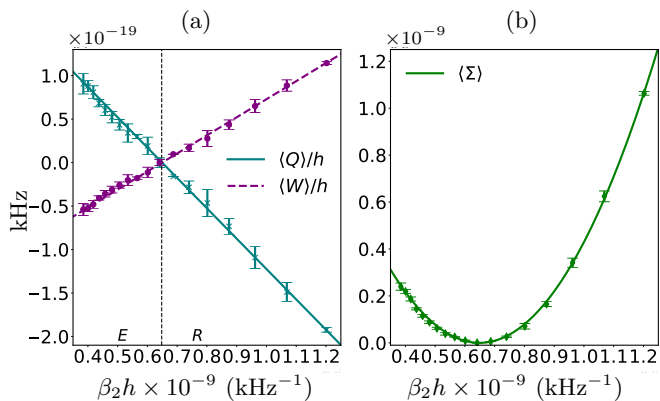


FIG. 4. Plots depicting dynamics of the direct SWAP engine. (a) Average heat and work values for different spin temperatures of the second qubit, keeping the value of the inverse spin temperature of the first qubit fixed at $\beta_1 h = 1.61 \times 10^{-10} \text{ kHz}^{-1}$. Theoretically calculated average values of heat and work are shown as solid teal and dashed purple lines, respectively. The experimentally obtained values (with error bars) are shown as teal crosses and purple circles, respectively. The SWAP engine functions as a heat engine in the region to the left of the dashed vertical line and as a refrigerator in the region to the right of the dashed vertical line. (b) Average value of entropy ($\langle \Sigma \rangle$). The theoretical prediction is depicted by a solid green line and the experimental values (with error bars) are shown as green diamonds.

B. PPS SWAP Engine Dynamics

The direct SWAP engine implementation method offers the advantage that the nuclei are already in the Gibbs thermal state, which can be used as an initial state. Furthermore, it can be calculated that using the direct SWAP engine method, $\approx 6.023 \times 10^{23}$ spins participate in the engine dynamics whereas using the PPS SWAP engine, a much lower number $\approx 7.287 \times 10^{18}$ spins participate in the engine dynamics. While the engine dynamics in different working regimes can be easily captured by using the direct SWAP engine, the entropy produced by this engine is very low. Our numerical calculations showed that violation of TUR-1 occurs for spin temperature values lower than $0.266 \mu\text{K}$ for the second qubit. Hence, despite the easier implementation protocol of the direct SWAP engine, we decided to use the PPS SWAP engine to study the violation of TUR-1 and TUR-2.

To study the dynamics of the PPS SWAP engine and explore the validity of the TURs, we keep the inverse spin temperature $\beta_1 h$ of the first qubit fixed at two different values namely, at $0.177(\text{kHz}^{-1})=0.271 \mu\text{K}$ and at $0.289(\text{kHz}^{-1})=0.165 \mu\text{K}$. The inverse spin temperature $\beta_2 h$ of second qubit is varied, which allows us to investigate the engine dynamics at different spin temperatures. We plotted the average irreversible entropy ($\langle \Sigma \rangle$), average work ($\langle W \rangle$) and heat ($\langle Q \rangle$) as a function of $\beta_2 h$ in Figure 5. From the top plots of Figure 5, it can be inferred that $\langle \Sigma \rangle \geq 0$, which can be regarded as recasting of the sec-

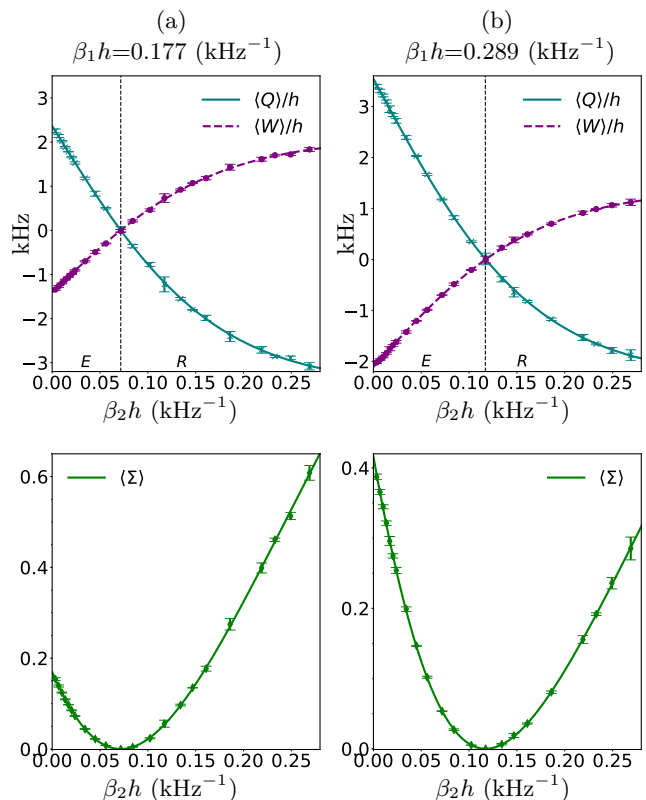


FIG. 5. Plots depicting dynamics of the PPS SWAP engine. Top plots in panels (a) and (b) depict average heat and work values for different spin temperatures of the second qubit, keeping the value of the inverse spin temperature of the first qubit fixed at $\beta_1 h = 0.177 \text{ kHz}^{-1}$ and $\beta_1 h = 0.289 \text{ kHz}^{-1}$, respectively. Theoretically calculated average values of heat and work are shown as solid teal and dashed purple lines, respectively. The experimentally obtained values (with error bars) are shown as teal crosses and purple circles, respectively. The SWAP engine functions as a heat engine in the region to the left of the dashed vertical line and as a refrigerator in the region to the right of the dashed vertical line. Bottom plots in panels (a) and (b) depict the average value of entropy ($\langle \Sigma \rangle$) at the two fixed inverse spin temperature of the first qubit. The theoretical prediction is depicted by a solid green line and the experimental values (with error bars) are shown as green diamonds.

ond law of thermodynamics for the stochastic regime at the microscopic level. This is a confirmation of the second law for a non-equilibrium thermodynamic process. When the energy gap ratio of both qubits is the same as their spin temperature ratio ($\frac{\epsilon_1}{\epsilon_2} = \frac{\beta_2}{\beta_1}$), the average heat and work are zero, and hence the average entropy change is also zero. At this point, both the work and heat curves cross each other. We obtain a very good agreement between our experimental values and the theoretical predictions as shown in Figure 5.

Work is extracted ($\langle W \rangle < 0$) from the quantum SWAP engine and it functions as a heat engine when $\beta_2 < (\epsilon_1/\epsilon_2)\beta_1$. This can be observed from the bottom

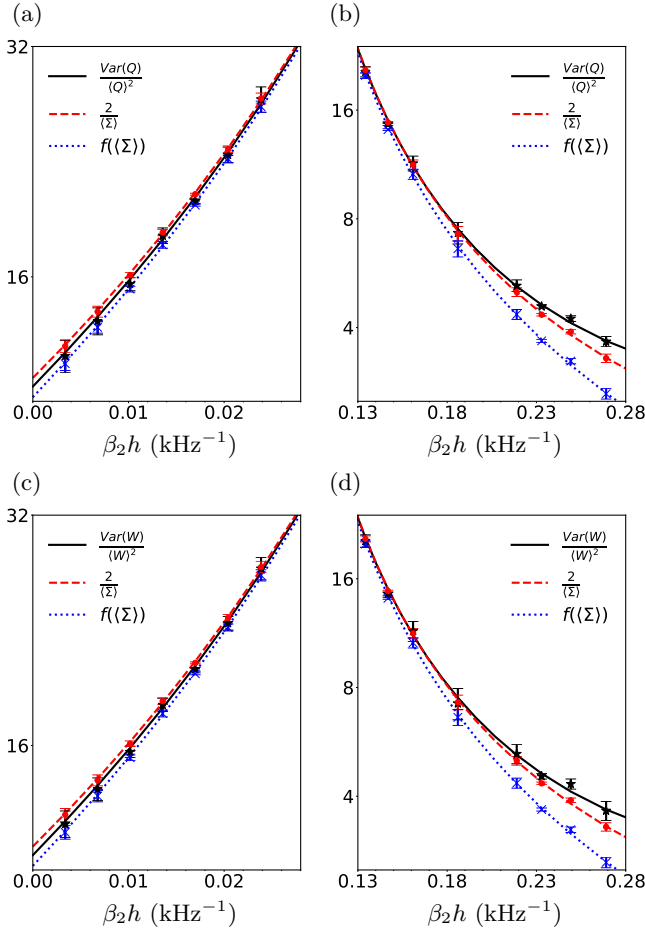


FIG. 6. Comparison between TUR bounds. The $\beta_1 h$ value of the first qubit is kept fixed at $0.177 \text{ (kHz}^{-1}\text{)}$ and spin temperatures of the second qubit are plotted on the x -axis. Inverse noise-to-signal ratio, TUR-1 and TUR-2 are depicted with a solid black, a dashed red and a dotted blue line, respectively and their experimental values (with error bars) are shown with black stars, red circles and blue crosses, respectively. Plots (a) and (c) depict the heat engine regime while plots (b) and (d) depict the refrigerator regime for heat and work of inverse noise-to-signal ratio. A violation of TUR-1 is observed in the heat engine regime, while TUR-2 is always valid in every parameter space. Inverse noise-to-signal ratio is the same for heat and work, which can be observed by comparing plot (a) with (c) and plot (b) with (d).

plots of Figure 5. The condition for the engine to work as a refrigerator is $\beta_2 > (\epsilon_1/\epsilon_2)\beta_1$, where work is consumed ($\langle W \rangle > 0$) from an external agent to make heat flow from a cold to a hot bath. The parameter space for the SWAP engine working as a heat engine and as a refrigerator is divided by a black dashed line shown in the bottom plots of Figure 5.

The ratios of the variances of heat and work to the square of their average values (LHS of TUR-1 and TUR-2) are plotted in Figures 6 and 7 as solid black lines. This inverse signal-to-noise ratio is compared with the TUR-1 and TUR-2 bounds (depicted as dotted red and dashed

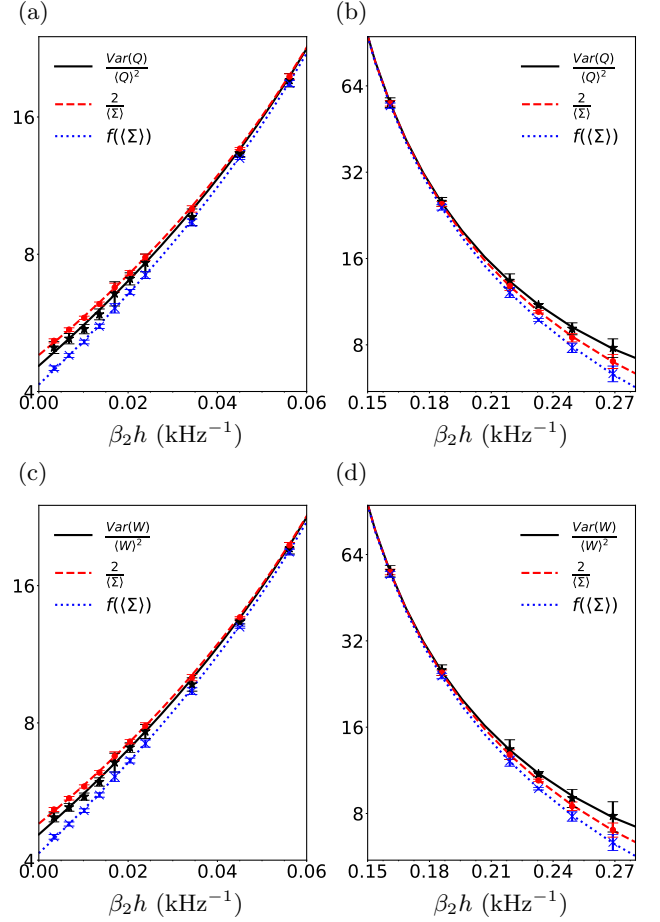


FIG. 7. Same as Figure 6, but with the spin temperature of qubit 1 kept fixed at $\beta_1 h = 0.289 \text{ (kHz}^{-1}\text{)}$.

blue curves, respectively). The experimental data points (with error bars) are shown in the same colors as their respective theoretical predictions. For small entropy production limits ($\langle \Sigma \rangle \approx 0$) the TUR-2 bound reduces to the TUR-1 bound, which can be seen as all three lines are merging into one single line as we move towards the $\beta_2 h$ values which have nearly zero entropy. As evident from Figures 6 and 7, TUR-2 is always satisfied as it is derived from the XFT scenario (which includes the quantum SWAP engine). A violation of the TUR-1 bound is observed in the heat engine regime. The violation of TUR-1 is directly proportional to the entropy production in the SWAP engine. When the average entropy production is increased in the heat engine regime, the violation becomes more significant (the dotted red curve is above the solid black curve). In the refrigerator regime, it is observed that both the bounds weaken as the entropy production is increased. This could open up the possibility of a new TUR which is tighter than TUR-2 for XFT cases.

V. CONCLUSIONS

We used an NMR quantum processor to implement a quantum SWAP engine using two different methods, namely, a direct method and a PPS method. The direct method is easier to implement experimentally and exploits the fact that the spins are already in the Gibbs thermal state, which itself can then be used as the initial thermal state. The quantum SWAP engine was characterized in its working regimes as an engine and a refrigerator, depending on its initial equilibrium state.

Further, we explored the validity of the TURs using a quantum SWAP engine implemented via the PPS SWAP engine method. Our results indicate that the irreversible entropy production is always nonzero, which follows the second law of thermodynamics at the stochastic level. We obtained a very good match between the theoretical calculations and the experimental results, which validates using NMR quantum processors as heat engines at

the microscopic level. Two different bounds on inverse noise-to-signal ratio, which were derived using different physical scenarios, were explored. We experimentally studied these bounds and verified that TUR-2 is always valid in every working parameter space of the quantum SWAP engine, while TUR-1 is violated in certain working regimes of the quantum SWAP engine. Our study is a step forward in the emerging field of experimental explorations of non-equilibrium quantum thermodynamics.

ACKNOWLEDGMENTS

All experiments were performed on a Bruker Avance-III 600 MHz NMR spectrometer at the NMR Research Facility at IISER Mohali. K. S. acknowledges financial support from the Prime Minister's Research Fellowship (PMRF) scheme of the Government of India.

-
- [1] J. Goold, M. Huber, A. Riera, L. del Rio, and P. Skrzypczyk, *Journal of Physics A: Mathematical and Theoretical* **49**, 143001 (2016).
 - [2] S. Vinjanampathy and J. Anders, *Contemporary Physics* **57**, 545 (2016).
 - [3] Y. Zou, Y. Jiang, Y. Mei, X. Guo, and S. Du, *Phys. Rev. Lett.* **119**, 050602 (2017).
 - [4] J. Klatzow, J. N. Becker, P. M. Ledingham, C. Weinzetl, K. T. Kaczmarek, D. J. Saunders, J. Nunn, I. A. Walmesley, R. Uzdin, and E. Poem, *Phys. Rev. Lett.* **122**, 110601 (2019).
 - [5] C. Jarzynski, *Phys. Rev. Lett.* **78**, 2690 (1997).
 - [6] G. E. Crooks, *Phys. Rev. E* **60**, 2721 (1999).
 - [7] C. Jarzynski and D. K. Wójcik, *Phys. Rev. Lett.* **92**, 230602 (2004).
 - [8] M. Campisi, P. Hänggi, and P. Talkner, *Rev. Mod. Phys.* **83**, 771 (2011).
 - [9] M. Campisi, *Journal of Physics A: Mathematical and Theoretical* **47**, 245001 (2014).
 - [10] T. B. Batalhão, A. M. Souza, L. Mazzola, R. Auccaise, R. S. Sarthour, I. S. Oliveira, J. Goold, G. De Chiara, M. Paternostro, and R. M. Serra, *Phys. Rev. Lett.* **113**, 140601 (2014).
 - [11] S. Pal, T. S. Mahesh, and B. K. Agarwalla, *Phys. Rev. A* **100**, 042119 (2019).
 - [12] K. Micadei, J. P. S. Peterson, A. M. Souza, R. S. Sarthour, I. S. Oliveira, G. T. Landi, R. M. Serra, and E. Lutz, *Phys. Rev. Lett.* **127**, 180603 (2021).
 - [13] T. Denzler, J. F. G. Santos, E. Lutz, and R. M. Serra, *Quantum Science and Technology* **9**, 045017 (2024).
 - [14] S. An, J.-N. Zhang, M. Um, D. Lv, Y. Lu, J. Zhang, Z.-Q. Yin, H. T. Quan, and K. Kim, *Nature Physics* **11**, 193 (2015).
 - [15] S. Hernández-Gómez, N. Staudenmaier, M. Campisi, and N. Fabbri, *New Journal of Physics* **23**, 065004 (2021).
 - [16] A. C. Barato and U. Seifert, *Phys. Rev. Lett.* **114**, 158101 (2015).
 - [17] P. Pietzonka, A. C. Barato, and U. Seifert, *Phys. Rev. E* **93**, 052145 (2016).
 - [18] A. C. Barato and U. Seifert, *Phys. Rev. X* **6**, 041053 (2016).
 - [19] J. M. Horowitz and T. R. Gingrich, *Nature Physics* **16**, 15 (2020).
 - [20] K. Ptaszyński, *Phys. Rev. B* **98**, 085425 (2018).
 - [21] B. K. Agarwalla and D. Segal, *Phys. Rev. B* **98**, 155438 (2018).
 - [22] J. Liu and D. Segal, *Phys. Rev. E* **99**, 062141 (2019).
 - [23] A. M. Timpanaro, G. Guarnieri, J. Goold, and G. T. Landi, *Phys. Rev. Lett.* **123**, 090604 (2019).
 - [24] S. Pal, S. Saryal, D. Segal, T. S. Mahesh, and B. K. Agarwalla, *Phys. Rev. Res.* **2**, 022044 (2020).
 - [25] H. T. Quan, Y.-x. Liu, C. P. Sun, and F. Nori, *Phys. Rev. E* **76**, 031105 (2007).
 - [26] R. Uzdin, A. Levy, and R. Kosloff, *Phys. Rev. X* **5**, 031044 (2015).
 - [27] J. P. S. Peterson, T. B. Batalhão, M. Herrera, A. M. Souza, R. S. Sarthour, I. S. Oliveira, and R. M. Serra, *Phys. Rev. Lett.* **123**, 240601 (2019).
 - [28] R. J. de Assis, T. M. de Mendonça, C. J. Villas-Boas, A. M. de Souza, R. S. Sarthour, I. S. Oliveira, and N. G. de Almeida, *Phys. Rev. Lett.* **122**, 240602 (2019).
 - [29] V. F. Lisboa, P. R. Dieguez, J. R. Guimarães, J. F. G. Santos, and R. M. Serra, *Phys. Rev. A* **106**, 022436 (2022).
 - [30] J. Klatzow, J. N. Becker, P. M. Ledingham, C. Weinzetl, K. T. Kaczmarek, D. J. Saunders, J. Nunn, I. A. Walmesley, R. Uzdin, and E. Poem, *Phys. Rev. Lett.* **122**, 110601 (2019).
 - [31] J. Roßnagel, S. T. Dawkins, K. N. Tolazzi, O. Abah, E. Lutz, F. Schmidt-Kaler, and K. Singer, *Science* **352**, 325 (2016).
 - [32] G. Maslennikov, S. Ding, R. Hablützel, J. Gan, A. Roulet, S. Nimmrichter, J. Dai, V. Scarani, and D. Matsukevich, *Nature Communications* **10**, 202 (2019).
 - [33] A. Solfanelli, A. Santini, and M. Campisi, *PRX Quantum* **2**, 030353 (2021).
 - [34] K. Huang, C. Xi, X. Long, H. Liu, Y.-a. Fan, X. Wang, Y. Zheng, Y. Feng, X. Nie, and D. Lu, *Phys. Rev. Lett.*

- 132**, 210403 (2024).
- [35] M. Herrera, J. H. Reina, I. D'Amico, and R. M. Serra, *Phys. Rev. Res.* **5**, 043104 (2023).
- [36] M. Campisi, J. Pekola, and R. Fazio, *New Journal of Physics* **17**, 035012 (2015).
- [37] M. A. Nielsen and I. L. Chuang, *Quantum Computation and Quantum Information* (Cambridge University Press, Cambridge UK, 2010).
- [38] M. F. Sacchi, *Phys. Rev. A* **104**, 012217 (2021).
- [39] L. M. K. Vandersypen and I. L. Chuang, *Rev. Mod. Phys.* **76**, 1037 (2005).
- [40] I. S. Oliveira, T. J. Bonagamba, R. S. Sarthour, J. C. C. Freitas, and E. R. deAzevedo, *NMR quantum information processing* (Elsevier Science B.V., Amsterdam, 2007).
- [41] A. Gaikwad, Arvind, and K. Dorai, *Quantum Information Processing* **20**, 19 (2021).
- [42] J. Zhang, A. M. Souza, F. D. Brandao, and D. Suter, *Phys. Rev. Lett.* **112**, 050502 (2014).